ACS NANO

www.acsnano.org

ARTICLE

Self-Activated Catalytic Sites on Nanoporous Dilute Alloy for High-Efficiency Electrochemical Hydrogen Evolution

Yaqian Yu,[‖] Kang Jiang,[‖] Min Luo,[‖] Yang Zhao, Jiao Lan, Ming Peng, Frank M. F. de Groot, and Yongwen Tan*

Cite This: *ACS Nano* 2021, 15, 5333−5340

Read Online

ACCESS | Metrics & More | Article Recommendations | Supporting Information

ABSTRACT: **Design and synthesis of effective electrocatalysts for hydrogen evolution reaction (HER) in wide pH environments are critical to reduce energy losses in water electrolyzers. Here, by using a self-activation strategy, we construct an atomic nickel (Ni) decorated nanoporous iridium (Ir) catalyst, which can create the reaction-favorable chemical environment and maximize the electrochemical active surface area (ECSA), enabling efficient HER over a wide pH range. By using *operando* X-ray absorption spectroscopy and theoretical calculations, the atomic Ni sites are identified as the synergistic sites, which not only accelerate the water dissociation under operation conditions but also activate the surface Ir sites thus leading to the efficient H_2 generation. This work highlights the significance of atomic-level decorating strategy which can optimize the activity of surface Ir atoms with negligible sacrifice of the ECSA.**

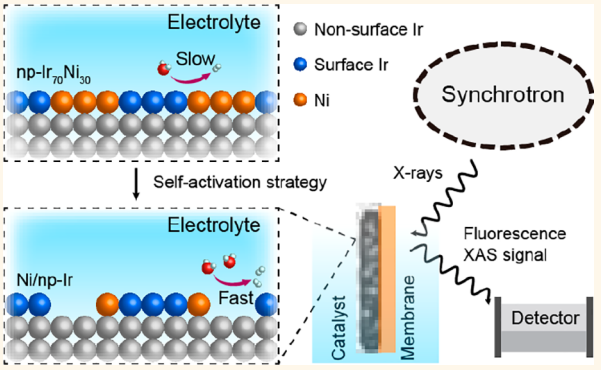

KEYWORDS: *nanoporous metal, dealloying, atomic engineering, hydrogen evolution reaction, synergistic effect, operando X-ray absorption spectroscopy*

The large-scale storage of renewable energy sources, such as wind or solar energy, is a pressing need to alleviate the aggravated global energy crisis while addressing the environmental issues. Hydrogen is an attractive energy carrier due to its high energy density and pollution-free gas emission, which is vital for developing green energy technologies.[1] Electrocatalytic water splitting is one of the most effective ways to produce H_2 to meet the demands in which HER occurs at the cathode.[2−17] Pt is regarded as the most active electrocatalyst for HER in acidic media, yet its catalytic kinetics become slower when the working environment transferred from the acidic to the alkaline.[11,18] For improving the reliability during operation, it is highly desirable to develop a high-performance catalyst that is universally compatible (e.g., catalysts that can perform well in a wide pH range) so as to enable a mass of electrolytes to be directly used for hydrogen generation.

Alloying has been emerging as an efficient strategy to tune the electronic and geometric features of noble metals and optimize their catalytic active centers in which the adsorption/desorption properties of the relevant reaction species can be altered to achieve the ideal catalytic performance.[3−5,19−21] Adding transition metal can enhance the catalytic performance of noble metal via ligand effect through modifying the binding strength of intermediates,[4,5,22] but it inevitably blocks some surface-active sites of noble metal and often sacrifices the electrochemical active surface area (ECSA). In this regard, it is important to minimize the size of the decorating species to prevent unnecessary blockage of surface-active sites while creating the most activated sites with decorating species. The ultimate limit of the decorating species is the use of isolated atoms, which allow the smallest number of decorating species to activate the most atoms of noble metal supports, thus ensuring the highest ECSA.[23,24] Meanwhile, the isolated decorating atoms possessing the refined coordination geometry offer an ideal model for exploring the synergistic effect between noble metal support and the isolated decorating atoms under realistic reaction conditions.[6,25] However, *operando* monitoring

Received: December 29, 2020
Accepted: February 26, 2021
Published: March 3, 2021

https://dx.doi.org/10.1021/acsnano.0c10885
ACS Nano 2021, 15, 5333−5340

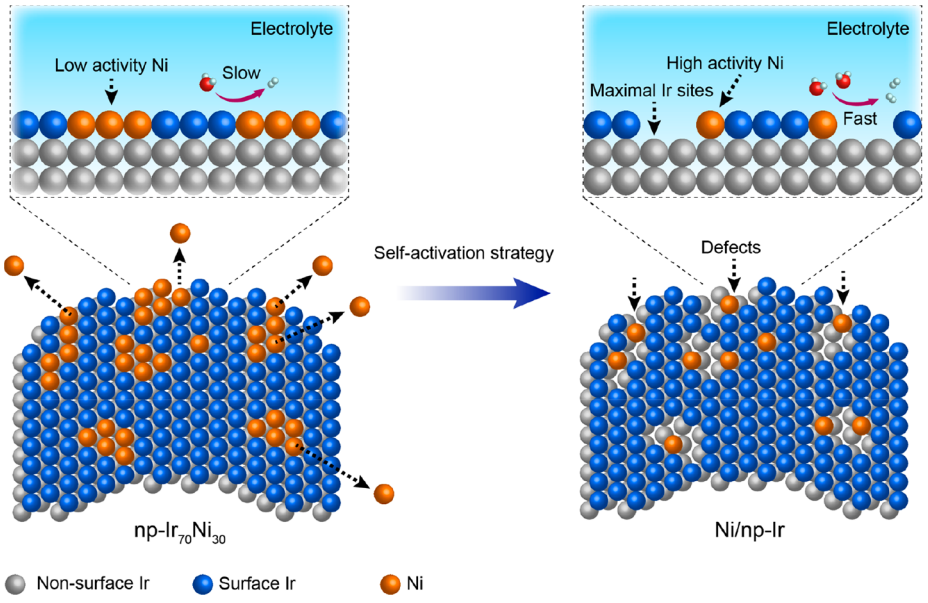

Figure 1. Schematic illustration for the preparation of Ni/np-Ir.

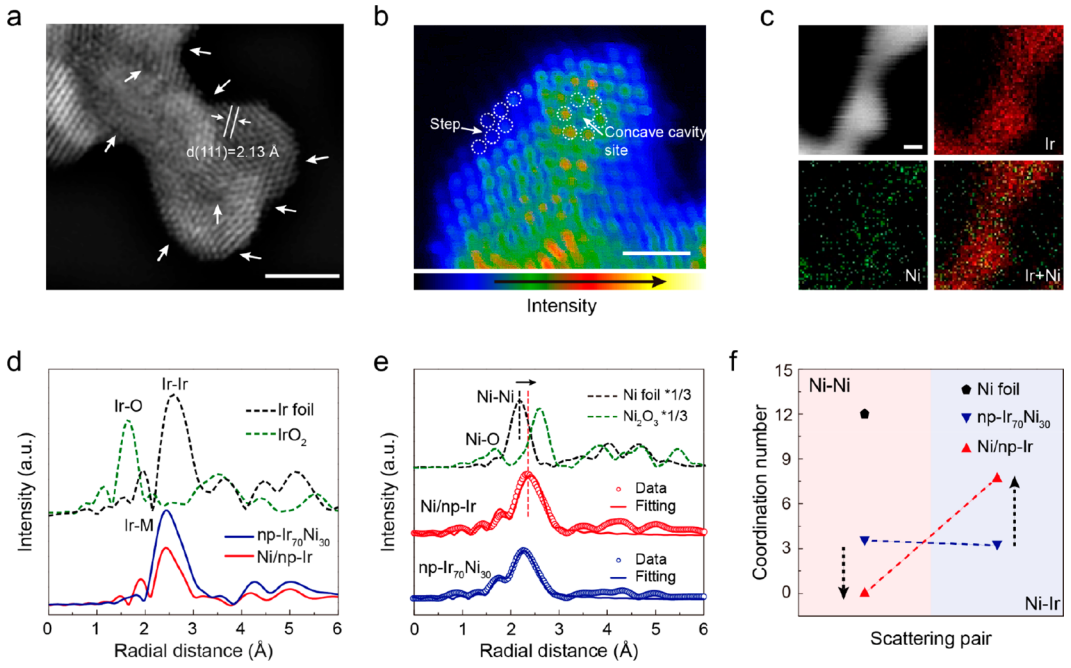

Figure 2. Structural characterizations of the Ni/np-Ir. (a) HAADF-STEM image of Ni/np-Ir. White arrows represent the defects, steps, and concave cavity sites on the surface. (b) Magnified HAADF-STEM image of Ni/np-Ir. (c) The EDX elemental mapping of Ni/np-Ir. (d) The Ir L_3-edge FT-EXAFS spectra. (e) The Ni K-edge FT-EXAFS spectra and corresponding EXAFS fitting results. (f) First-shell (Ni−Ir) FT-EXAFS fitting results of Ni/np-Ir. Scale bars: (a) 5 nm. (b) 1 nm. (c) 50 nm.

the dynamic behaviors of isolated decorating atoms and identifying its synergistic effect with noble metal supports under realistic reaction conditions are rarely available yet are pivotal for the development of efficient catalysts.[7,26,27]

Herein, we present a self-activation strategy to obtain an atomic Ni decorated bicontinuous nanoporous iridium catalyst (denoted as Ni/np-Ir). Benefiting from the maximized ECSA and the modification of isolated Ni atoms, the resulting Ni/np-Ir exhibits extraordinary catalytic performance with near-zero onset potential, ultralow Tafel slope, and high price activity over a wide pH range for the HER, surpassing the state-of-the-art catalysts and commercial catalysts (Pt/C and Ir/C). *Operando* X-ray absorption spectroscopy (XAS) and density functional theory (DFT) calculations, taken together, reveal that the atomic Ni sites not only act as highly active sites for water dissociation under realistic reaction conditions but also modulate the electronic structure of Ir sites thus lowering the energy barriers of H−H coupling. These works demonstrate the feasibility of using atomic-level decorating sites to tune the intrinsic activity of the catalyst for HER and provide a deep understanding in the synergistic effect of isolated decorating sites.

https://dx.doi.org/10.1021/acsnano.0c10885
ACS Nano 2021, 15, 5333−5340

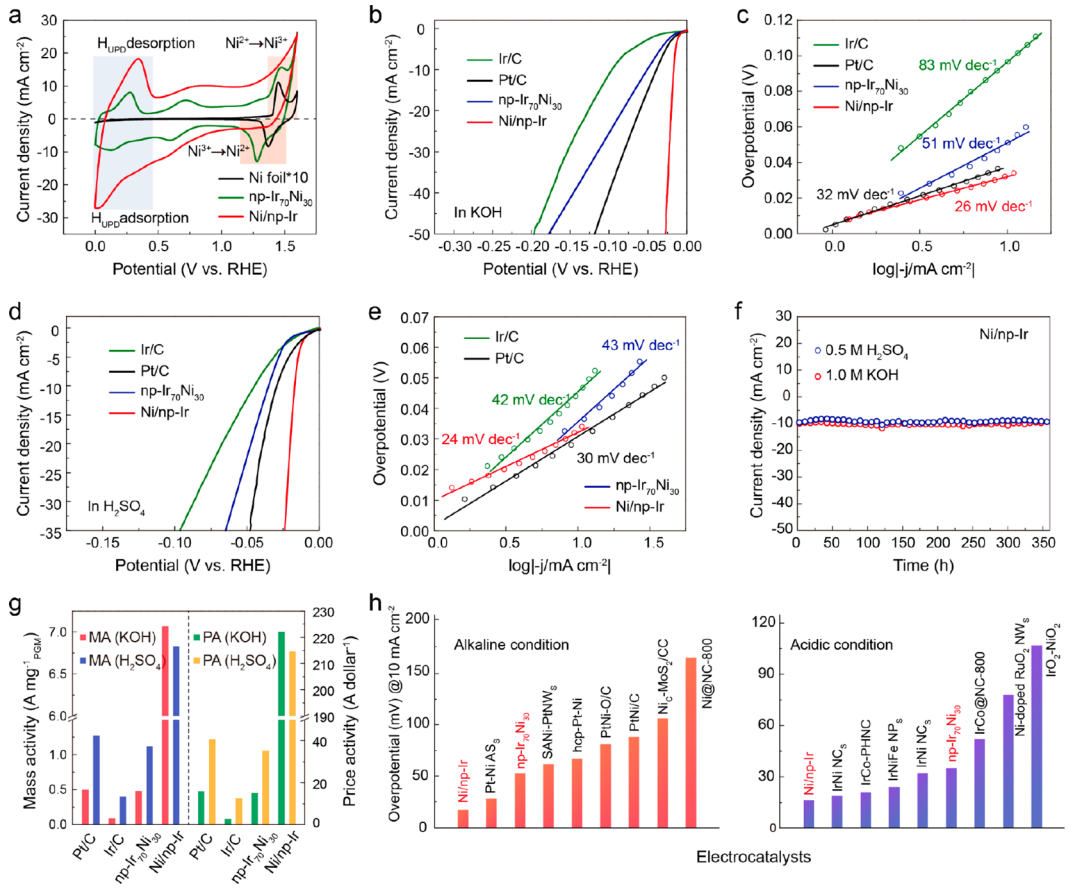

Figure 3. Electrochemical HER performance. (a) CV curves of Ni/np-Ir, np-$Ir_{70}Ni_{30}$, and Ni foil. (b) HER polarization curves of Ni/np-Ir, np-$Ir_{70}Ni_{30}$, Pt/C, and Ir/C in 1.0 M KOH. (c) Corresponding Tafel plots of (b). (d) HER polarization curves of Ni/np-Ir, np-$Ir_{70}Ni_{30}$, Pt/C, and Ir/C in 0.5 M H_2SO_4. (e) The corresponding Tafel plots of (d). (f) Chronoamperometry curves of Ni/np-Ir obtained at an overpotential of 20 mV in 1.0 M KOH and 17 mV in 0.5 M H_2SO_4. (g) Mass activity and price activity of Pt/C, Ir/C, np-$Ir_{70}Ni_{30}$, and Ni/np-Ir at an overpotential of 50 mV. (h) The comparison of HER overpotentials at a current density of 10 mA cm^{-2} in different Ir-based catalysts in alkaline and acidic condition.

RESULTS AND DISCUSSION

Synthesis and Characterizations. The Ir_3Ni_{97} alloy ribbons were synthesized by an arc melting and single-roller melt spinning method. Then, an electrochemically dealloying method was used to obtain nanoporous $Ir_{70}Ni_{30}$ alloy (denoted as np-$Ir_{70}Ni_{30}$; more experimental details are shown in Supporting Information). The self-activation process was conducted by performing repeated cyclic voltammetry (CV) scans between 0.0 and 0.7 V versus reversible hydrogen electrode (RHE) in 0.25 M HCl to gradually remove nickel species (Figure 1, Figure S1−S3), manifesting as the vanishing of the Ni characteristic peak and the increase of underpotentially deposited H (H_{UPD}) desorption area. Simultaneously, the ECSA gradually increases with the number of CV cycles and finally reaches the maximum after 500 CV cycles, indicating that the decorated Ni species gradually become stable (Figure S4 and Figure S5).

The X-ray diffraction (XRD) pattern of np-$Ir_{70}Ni_{30}$ consists of Ni-enriched and Ir-enriched phases. During the self-activation process, the diffraction peaks of the Ni-enriched phase gradually weakened and disappeared while the diffraction peaks of Ir-enriched phase show a negative shift close to Ir, which is a preliminary prediction of the formation of the atomic Ni decorated nanoporous iridium catalyst (Figure S6). By virtue of HER as a model reaction, it is discovered that the material produced with 500 CV cycles displays the best HER performance (Figure S2b). Therefore, we will focus the discussion on this material. The scanning electron microscope (SEM) image displays the three-dimensional microwires' morphology of Ni/np-Ir (Figure S7). The bicontinuous nanoporous structure in the microwires of Ni/np-Ir is revealed by high-angle annular dark-field scanning transmission electron microscopy (HAADF-STEM) (Figure S8). Notably, it is distinct that abundant vacancy defects, concave cavity sites, and atomic steps exist on (111) planes of cubic Ir crystal (2.13 Å, close to 2.19 Å in the JCPDS No. 01-1216) (Figure 2a,b).[28] The STEM energy dispersive X-ray spectroscopy (STEM-EDX) elemental mapping analyses further highlight the homogeneous distribution of Ni and Ir atoms across the analyzed zone (Figure 2c).

X-ray absorption near-edge structure (XANES) spectroscopy and extended X-ray absorption fine structure (EXAFS) spectroscopy were performed to further probe the electronic structures and coordination environments of Ni/np-Ir. The Ir L_3-edge XANES spectra of np-$Ir_{70}Ni_{30}$ and Ni/np-Ir exhibit the same feature peaks (Peak I, Peak II, and Peak III) with Ir foil, indicating the metallic property of Ir in np-$Ir_{70}Ni_{30}$ and Ni/np-Ir (Figure S9a), which is consistent with XPS results (Figure S10). The corresponding Fourier transform of the EXAFS (FT-EXAFS) spectrum of np-$Ir_{70}Ni_{30}$ exhibits a prominent

https://dx.doi.org/10.1021/acsnano.0c10885
ACS Nano 2021, 15, 5333−5340

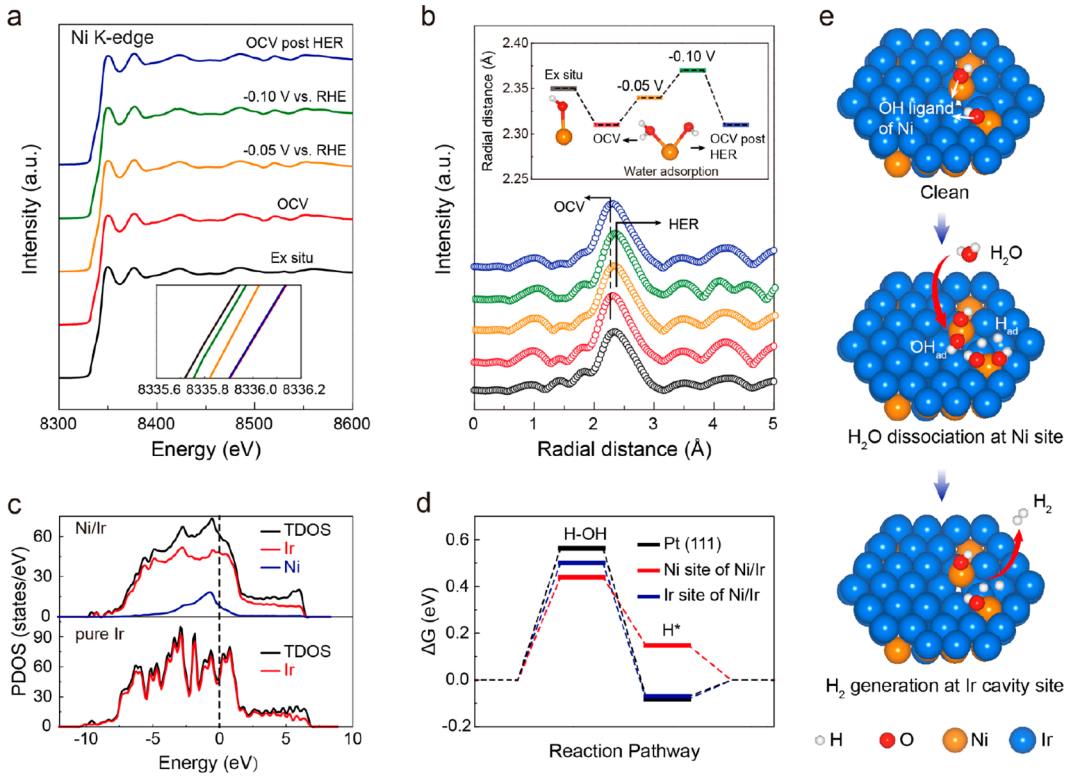

Figure 4. ***Operando*** **XAS characterizations and theoretical investigations for Ni/np-Ir. (a) The Ni K-edge XANES spectra of Ni/np-Ir obtained under different applied voltages in 1.0 M KOH. Inset shows the magnified pre-edge region. (b) The corresponding FT-EXAFS spectra from (a). Inset shows the variation of the Ni−Ir scattering feature. (c) Calculated PDOS of Ni/Ir and pure Ir. (d) Free energy diagrams of HER. (e) Schematic illustration of the HER mechanism on Ni/Ir.**

peak at ∼2.4 Å, corresponding to the overlapping of the Ir−Ir and Ir−Ni scattering feature (Figure 2d).[29] However, the same characteristic peak in the FT-EXAFS spectrum of Ni/np-Ir is evidently lower than that of np-$Ir_{70}Ni_{30}$, indicating the decrease of the coordination number of Ir−Ir and Ir−Ni bonds (Figure S9b).[8] This further confirms the formation of abundant defects on the surface of Ni/np-Ir, in accordance with the HAADF-STEM results. The Ni K-edge XANES spectra of np-$Ir_{70}Ni_{30}$ and Ni/np-Ir are situated between those of Ni foil and Ni_2O_3, indicating the partial oxidation of surface Ni during the corrosion process (Figure S9c). The corresponding FT-EXAFS spectrum of np-$Ir_{70}Ni_{30}$ shows a prominent peak located between Ni−Ni and Ir−Ir scattering peaks, revealing the alloy feature of np-$Ir_{70}Ni_{30}$ (Figure 2e).[29,30] Significantly, the corresponding FT-EXAFS spectrum of Ni/np-Ir displays the high-*R* shift of the prominent peak compared with that of np-$Ir_{70}Ni_{30}$, namely, much closer to the Ir−Ir scattering peak (Figure 2e and Figure S9d,e). Structural information about local atomic coordination was further inferred by fitting EXAFS spectra with the fitted structural parameters (Figure 2f and Table S1) in which only the Ni−Ir bond at ∼2.6 Å with an average coordination number of 7.9 in Ni/np-Ir is observed without any contribution from the Ni−Ni bond.[31] This indicates that Ni atoms are incorporated into the crystal lattice of Ir in Ni/np-Ir, underscoring the atomic nature of Ni.[32,33] Figure 3a shows the CV curves of the Ni/np-Ir, np-$Ir_{70}Ni_{30}$, and Ni foil in Ar-saturated 1.0 M KOH solution. The peaks at 1.29 and 1.47 V versus RHE could be attributed to the redox couple of Ni, which is defined as a signature of Ni crystal.[23] For Ni/np-Ir, the absence of characteristic peaks for Ni crystal indicates the removal of bulk Ni species, which further confirms that the Ni species are atomically dispersed in Ni/np-Ir.[7,9] Meanwhile, the hydrogen absorption−desorption peaks of Ni/np-Ir is distinctly higher than that of np-$Ir_{70}Ni_{30}$, emphasizing the maximum ECSA in Ni/np-Ir.[23]

Electrochemical HER Performance. The HER performance of the Ni/np-Ir and np-$Ir_{70}Ni_{30}$ was measured through linear sweep voltammetry (LSV) in Ar-saturated 1.0 M KOH and 0.5 M H_2SO_4 solutions with a standard three-electrode setup at a scan rate of 1.0 mV s^{-1} along with commercial Ir/C and Pt/C as references. As shown in Figure 3b, the Ni/np-Ir exhibits the highest HER performance among these catalysts which only require an extremely low overpotential of 20 mV to achieve a current density of 10 mA cm^{-2} in 1.0 M KOH, significantly smaller than those of np-$Ir_{70}Ni_{30}$, Pt/C, and Ir/C. A small Tafel slope of 26 mV per decade (mV dec^{-1}) is measured for Ni/np-Ir (Figure S11a,b), which is much lower than those of np-$Ir_{70}Ni_{30}$ (51 mV dec^{-1}), Pt/C (32 mV dec^{-1}), and Ir/C (83 mV dec^{-1}) (Figure 3c), indicating the high intrinsic activity of Ni/np-Ir. Also shown are the polarization curves of np-$Ir_{70}Ni_{30}$ and Ni/np-Ir normalized by the ECSA, which show that the Ni/np-Ir possesses much larger current density than those of np-$Ir_{70}Ni_{30}$, Pt/C, and Ir/C (Figure S12). Apparently, Ni/np-Ir has the highest specific activity for HER under similar experimental measurement conditions. The electrochemical impedance spectroscopy (EIS) measurements of Ni/np-Ir further indicates that the Ni/np-Ir possesses smaller internal resistance and faster charge transfer behavior than np-$Ir_{70}Ni_{30}$ (Figure S13), thus realizing a rapid HER kinetics. Besides, the turnover frequencies (TOF) of Ni/np-Ir at some representative potential were calculated, which is better than that of np-$Ir_{70}Ni_{30}$ (Figure S14). In addition to the

https://dx.doi.org/10.1021/acsnano.0c10885
ACS Nano 2021, 15, 5333−5340

basic solution, Ni/np-Ir is also highly active toward HER in acidic electrolyte, delivering an overpotential of 17 mV to achieve a current density of 10 mA cm^{-2}, which is much lower than those of np-$Ir_{70}Ni_{30}$, Pt/C, and Ir/C (Figure 3d). Correspondingly, the Tafel slope of Ni/np-Ir is only 24 mV dec^{-1} (Figure S11c,d), which is much smaller than those of np-$Ir_{70}Ni_{30}$ (43 mV dec^{-1}), Pt/C (30 mV dec^{-1}), and Ir/C (42 mV dec^{-1}) (Figure 3e). Moreover, gas chromatography analyses show near 100% H_2 Faraday efficiency under different potentials for the Ni/np-Ir in 1.0 M KOH and 0.5 M H_2SO_4 solutions (Figure S15). The stability of Ni/np-Ir is assessed by a long-term chronoamperometry test, which shows an ignorable change of current density over 360 h (Figure 3f, and Figure S16).

Further insights into the stability of Ni/np-Ir by XAS and XPS measurement confirm that the Ni atoms keep atomic dispersion after long-term operation (Figures S17 and S18). Significantly, the Ni/np-Ir shows high mass activity (MA) of 7.07 A mg^{-1} in 1.0 M KOH and 6.83 A mg^{-1} in 0.5 M H_2SO_4 (Figure 3g and Figure S19). The price activity (PA) is also calculated (Table S2), which shows that Ni/np-Ir possesses high PA of 222.10 A $dollar^{-1}$ in 1.0 M KOH and 214.56 A $dollar^{-1}$ in 0.5 M H_2SO_4, far exceeding that of commercial Pt/C and Ir/C. By comparing with recently reported electrocatalysts, the Ni/np-Ir displays the competitive merits for HER, including overpotential at a current density of 10 mA cm^{-2}, Tafel slope, and stability (Figure 3h, Table S3, and Table S4).[10−14] Overall, these results unambiguously demonstrate that Ni/np-Ir is a highly versatile and efficient HER electrocatalyst in a wide pH range.

HER Enhancement Mechanism. In order to probe the role of an isolated Ni atom during the work conditions and to understand the origin of high catalytic activity, *operando* XAS measurements were performed to investigate the dynamic changes of atomic structure and oxidation state for Ni species in the Ni/np-Ir. During the *operando* XAS measurement, the potential was applied from open circuit voltage (denoted as OCV) to −0.10 V versus RHE and then back to OCV (Figure 4a).[7,27] The absorption edge of Ni/np-Ir in the XANES spectrum shifts to the higher energy side under OCV conditions as compared to that under *ex situ* condition (inset of Figure 4a), which suggests the adsorption of H_2O on Ni atoms,[19,34,35] resulting in the electron delocalization and the partial rearrangement of surface metal atoms, as also evidenced by the negative-shift of the Ni−Ir scattering peak in the corresponding FT-EXAFS spectrum (Figure 4b). However, when cathodic potentials of −0.05 and −0.10 V versus RHE were applied, the absorption edge of the Ni/np-Ir shifts to the lower energy side, implying the recovery of the low-oxidation-state Ni after H_2O dissociation occurs. This results from the greater speed of H_2O dissociation under realistic HER conditions, manifesting the fast H_2O dissociation processes on Ni atoms. Simultaneously, the occurrence of fast H_2O dissociation on Ni atoms also leads to the recovery of the initial surface atoms' arrangement, as reflected in the positive-shift of Ni−Ir scattering peak in the corresponding FT-EXAFS spectra. When the applied potential was set back to OCV, the absorption edge of Ni/np-Ir shifted back to the higher energy side along with the negative-shift of the Ni−Ir scattering peak. These indicate the restorability in the oxidation state and the arrangement of surface metal atoms in Ni/np-Ir. The *operando* XANES spectra at the Ir L_3-edge of the Ni/np-Ir were also shown to explain the dynamic changes of oxidation state for Ir species in the Ni/np-Ir. Under the applied potential, the oxidation state of Ir species decrease due to the reduction trend of the cathodic voltage under *operando* HER conditions, as evidenced by the decrease of the white line intensity (Figure S20a). The oxidation state of Ir species can reverse back to the initial oxidation state after the applied potential was set back to OCV, indicating the reversibility of oxidation state for Ir species. Moreover, no obvious change can be found from the corresponding FT-EXAFS spectra at different voltages (Figure S20b). These demonstrate the high stability of the oxidation state and local atomic structure for Ir species in Ni/np-Ir.

Density functional theory calculations based on the XAS-derived model were performed to provide further insights into the HER mechanism.[15] The inner Ni atoms were exhibited by replacing the inner Ir atoms while each surface Ni atom is coordinated with an O atom to achieve the partial oxidation. Figure 4c shows the projected density of states (PDOS) of Ni/np-Ir and pure Ir. The introduction of atomic Ni brings different hybridized electronic states in Ni/np-Ir which shows the higher occupied states than that of pure Ir near the Fermi level. This demonstrates that the decorating Ni atoms could optimize the electronic structure of Ir atoms, resulting in more excited electrons for the HER process. We then posited that the isolated Ni atoms and the Ir atoms at defect sites are the active sites for alkaline HER. It is distinct that the Ni sites show lower water adsorption energy than Ir sites, suggesting that Ni sites bear a strong water affinity (Figures S21 and S22).[16] Therefore, the Ni sites are preferential active sites for the adsorption of the H_2O molecule. Additionally, we calculated the reaction barrier of the Volmer step on different sites (Figure 4d, Figures S23 and S24) which show that Ni sites possess lower energy barrier of the Volmer step as compared to Ir sites, manifesting that Ni sites can easily activate H_2O molecules to generate intermediate H and OH species.[17] This result is in coincidence with the *operando* XAS analyses, further emphasizing the role of decorating Ni atoms on the accelerating rate-determining step (Volmer step) for alkaline HER.

Moreover, the Ir sites display lower energy barrier of H* adsorption as compared to Ni sites, suggesting that Ir sites are in charge of the coupling of H to H_2 during HER process. Combining with *operando* XAS analyses and DFT calculations, we put forward the straightforward mechanism for the high HER activity (Figure 4e). Under realistic reaction conditions, atomic Ni sites of Ni/np-Ir offer preferential sites for water adsorption and water dissociation, whereas Ir sites of Ni/np-Ir are in charge of the subsequent H* adsorption and the desorption of H_2.

CONCLUSIONS

In conclusion, we demonstrated that using self-activation strategy of atomic Ni species to engineer nanoporous Ir is an effective strategy to produce highly active and robust electrocatalysts for HER over a wide pH range. The resultant Ni/np-Ir shows superior HER performance as compared with the state-of-the-art catalysts and commercial catalysts. *Operando* XAS measurements and DFT calculations reveal that the decorated Ni sites not only act as active sites for accelerating the water dissociation process but also can tune the electronic structure of surface Ir sites, thus providing great accommodation for hydrogen adsorption/desorption and enabling the fast HER kinetics. This work highlights the importance of the isolated metal sites decorating approach for the HER, which

https://dx.doi.org/10.1021/acsnano.0c10885
ACS Nano 2021, 15, 5333−5340

can maximize the activity of decorating sites with minimal sacrifice of the ECSA. Additionally, this facile synthesis method can be scalable across a range of nanoporous dilute alloy systems, such as Ir−Co and Ir−Fe, thus achieving the fabrication of high-active electrocatalysts. Meanwhile, the synthesis method is environmentally friendly without large-scale use of organic solvents.

METHODS

Materials Synthesis. The Ir_3Ni_{97} alloy ingot was synthesized by arc melting and used as the mother alloy to fabricate Ir_3Ni_{97} alloy ribbons by single-roller melt spinning at a rotation rate of 3500 rpm. Then, the np-$Ir_{70}Ni_{30}$ was synthesized by electrochemical dealloying Ir_3Ni_{97} alloy ribbons at a voltage of 0.2 V versus Ag/AgCl in a 0.25 M HCl solution (about 1000 s). The dealloyed samples were cleaned by deionized water more than three times and dried in vacuum overnight. Subsequently, 2 mg of np-$Ir_{70}Ni_{30}$ was dispersed in a solution containing 0.5 mL of ethanol and 15 μL of 5 wt % Nafion solution by sonication for 1 h. Then, 10 μL of ink was dropped on a glassy carbon rotating disk electrode (RDE, geometrical area = 0.196 cm^2) for drying in the air. The self-activation process was conducted by performing repeated cyclic voltammetry (CV) scans (0, 100, 300, 500, 600 CV cycles) in 0.25 M HCl to gradually remove nickel species. The above catalysts with different CV cycles were denoted as np-$Ir_{70}Ni_{30}$, 100th, 300th, 500th, and 600th, respectively.

Structural Characterization. XRD patterns were recorded by using a Bruker D8 Advance X-ray diffraction with Cu Kα radiation (λ = 1.5418 Å). SEM experiments were conducted on Zeiss Sigma HD (Oxford EDS). HAADF-STEM images and EDX mappings were taken by a JEM-ARM 200F. The chemical state of the samples was carried out using XPS on Thermo Scientific ESCALAB250Xi spectrometer with monochromatic Al Kα. The content of Ir and Ni was obtained by ICP-OES on Agilent 730.

Electrochemical Measurement. The electrochemical tests were carried out on an electrochemical workstation (Ivium CompactStat. h) with a three-electrode cell at room temperature. A graphite rod and an Ag/AgCl electrode (or saturated calomel electrode, SCE) were used as the counter and reference electrode, respectively. In order to maximize the utilization efficiency of the catalysts, the catalysts were mixed with conductive carbon at a mass ratio of 15:85. For the preparation of catalysts' ink, 5 mg of mixed catalysts were dispersed in 5 mL of ethanol solution containing 100 μL of 5 wt % Nafion solution by sonication for 1 h. For Pt/C and Ir/C, 5 mg of Pt/C or Ir/C were dispersed in 5 mL ethanol solution containing 100 μL of 5 wt % Nafion solution by sonication for 1 h. Then, 30 μL of ink were dropped on a glassy carbon RDE with an area of 0.196 cm^2 for drying in the air. The loading values on RDE for np-$Ir_{70}Ni_{30}$, Ni/np-Ir, Pt/C, and Ir/C were 153.06 μg_{total} cm^{-2} (20.24 μg_{Ir} cm^{-2}), 153.06 μg_{total} cm^{-2} (22.09 μg_{Ir} cm^{-2}), 153.06 μg_{total} cm^{-2} (30.61 μg_{Pt} cm^{-2}), and 153.06 μg_{total} cm^{-2} (30.61 μg_{Ir} cm^{-2}). The polarization curves of HER were carried out in Ar-saturated 1.0 M KOH and 0.5 M H_2SO_4 solution with a scan rate of 1.0 mV s^{-1} and an electrode rotating of 1600 rpm. The data presented were *iR* corrected unless noted otherwise. The potential values shown were with respect to the reversible hydrogen electrode (RHE) by using following equations

$$E_{RHE} = E_{SCE} + 0.0591\ pH + 0.242\ V\ (in\ 1.0\ M\ KOH)$$

$$E_{RHE} = E_{Ag/AgCl} + 0.0591\ pH + 0.197\ V\ (in\ 0.5\ M\ H_2SO_4)$$

***Operando* XAS Measurements.** The Ir L_3-edge and Ni K-edge XAS spectra were recorded at the Beamline No. 01C1 in Taiwan Light Source. A three-electrode system (as described Electrochemical Measurements) was installed for the *operando* measurements. During the *operando* measurements, a series of HER-relevant potentials of OCV, −0.05 V, and −0.10 V versus RHE were applied to the working electrode. Simultaneously, the data were obtained in the fluorescence mode at room temperature.

DFT Calculations. All of the computations were performed by means of spin-polarized DFT methods using the Vienna *Ab initio* Simulation Package (VASP). The electron−electron exchange-correlation interaction was described with Perdew−Burke−Ernzerhof generalized gradient approximation (PBE-GGA) functional. The projector augmented wave (PAW) method was conducted to describe/treat interactions between the valence electrons and the ion cores. A cutoff energy of 450 eV was employed for the expansion of the wave functions. The IrNi structures were established according to the XAS fitting results and the (111) surface was chosen for adsorption according to the HAADF-STEM results. The atomic ratio of Ir/Ni in the unit cell was 90:10 according to the ICP results. The inner Ni atoms were exhibited by replacing the inner Ir atoms while each surface Ni atom is coordinated with an O atom to achieve the partial oxidation. A vacuum gap of 15 Å was imposed to avoid interactions between periodic images. All of the geometry is completely optimized until the total energy and atomic forces converged to 1×10^{-5} eV and 0.02 eV/Å, respectively. For the calculation of electronic properties, a k-point mesh of $5 \times 5 \times 1$ for supercell based on the Monkhorst−Pack scheme was used to sample the Brillouin zone. The Gibbs free energy change (ΔG) of each step was calculated by employing the standard hydrogen electrode (SHE) model. The ΔG can be calculated from $\Delta G = \Delta E + \Delta E_{ZPE} - T\Delta S$, where ΔE is the electronic energy change of the reactant and product species adsorbed on the catalyst surface obtained directly from DFT calculations, ΔE_{ZPE} is the difference in zero point energy, T is the temperature (T = 298.15 K), and ΔS is the entropy difference. The zero-point energies and entropies of the HER adsorbed species were computed by considering only the vibrational frequencies.

ASSOCIATED CONTENT

Supporting Information

The Supporting Information is available free of charge at https://pubs.acs.org/doi/10.1021/acsnano.0c10885.

Basic characterization of Ni/np-Ir and np-$Ir_{70}Ni_{30}$; supplementary XRD, SEM, and TEM images of samples; supplementary XANES and corresponding FT-EXAFS spectra of samples; supplementary XPS spectra of the Ni/np-Ir; supplementary electrocatalytic performance; supplementary structural parameter extracted from the Ni K-edge EXAFS fitting; comparison of the price for different noble metals; comparison of the catalytic HER performance of catalysts (PDF)

AUTHOR INFORMATION

Corresponding Author

Yongwen Tan − *College of Materials Science and Engineering, State Key Laboratory of Advanced Design and Manufacturing for Vehicle Body, Hunan University, Changsha, Hunan 410082, China;* orcid.org/0000-0003-1486-4048; Email: tanyw@hnu.edu.cn

Authors

Yaqian Yu − *College of Materials Science and Engineering, State Key Laboratory of Advanced Design and Manufacturing for Vehicle Body, Hunan University, Changsha, Hunan 410082, China*

Kang Jiang − *College of Materials Science and Engineering, State Key Laboratory of Advanced Design and Manufacturing for Vehicle Body, Hunan University, Changsha, Hunan 410082, China*

Min Luo − *Department of Physics, Shanghai Second Polytechnic University, Shanghai 201209, China*

Yang Zhao − *College of Materials Science and Engineering, State Key Laboratory of Advanced Design and*

https://dx.doi.org/10.1021/acsnano.0c10885
ACS Nano 2021, 15, 5333−5340

Manufacturing for Vehicle Body, Hunan University, Changsha, Hunan 410082, China

Jiao Lan − *College of Materials Science and Engineering, State Key Laboratory of Advanced Design and Manufacturing for Vehicle Body, Hunan University, Changsha, Hunan 410082, China*

Ming Peng − *College of Materials Science and Engineering, State Key Laboratory of Advanced Design and Manufacturing for Vehicle Body, Hunan University, Changsha, Hunan 410082, China;* orcid.org/0000-0002-8557-1202

Frank M. F. de Groot − *Inorganic Chemistry & Catalysis, Debye Institute for Nanomaterials Science, Utrecht University, 3584 CGUtrecht, The Netherlands;* orcid.org/0000-0002-1340-2186

Complete contact information is available at: https://pubs.acs.org/10.1021/acsnano.0c10885

Author Contributions

Y.W.T. conceived and supervised this study. Y.Q.Y., K.J., Y.Z., and J.L. carried out materials fabrication, XRD/SEM/XPS/ICP characterizations, and electrochemical measurements. M.L. performed the DFT calculations and computational models. K.J., M.P., Y.Q.Y., F.M.F.d.G. contributed to the XAS measurements and analyses of the XAS experiment results. Y.W.T., Y.Q.Y., and K.J. wrote the paper. All authors contributed to discussions and manuscript review.

Author Contributions

[‖]Y.Q.Y., K.J., and M.L. contributed equally to the work.

Notes

The authors declare no competing financial interest.

ACKNOWLEDGMENTS

This work was supported by the National Natural Science Foundation of China (Grant 51771072), the Youth 1000 Talent Program of China, Fundamental Research Funds for the Central Universities, the Outstanding Youth Scientist Foundation of Hunan Province (Grant 2020JJ2006), and Hunan University State Key Laboratory of Advanced Design and Manufacturing for Vehicle Body Independent Research Project (No. 71860007). The authors thank Y.-R. L. and T.-S. C. for the measurement of XAS at Beamline No. 01C1 of Taiwan Light Source.

REFERENCES

(1) Chu, S.; Majumdar, A. Opportunities and Challenges for a Sustainable Energy Future. *Nature* **2012**, *488*, 294−303.

(2) Stamenkovic, V. R.; Strmcnik, D.; Lopes, P. P.; Markovic, N. M. Energy and Fuels from Electrochemical Interfaces. *Nat. Mater.* **2017**, *16*, 57−69.

(3) Su, J.; Yang, Y.; Xia, G.; Chen, J.; Jiang, P.; Chen, Q. Ruthenium-Cobalt Nanoalloys Encapsulated in Nitrogen-Doped Graphene as Active Electrocatalysts for Producing Hydrogen in Alkaline Media. *Nat. Commun.* **2017**, *8*, 14969.

(4) Shan, J.; Ling, T.; Davey, K.; Zheng, Y.; Qiao, S. Z. Transition-Metal-Doped RuIr Bifunctional Nanocrystals for Overall Water Splitting in Acidic Environments. *Adv. Mater.* **2019**, *31*, 1900510.

(5) Wu, Q.; Luo, M.; Han, J.; Peng, W.; Zhao, Y.; Chen, D.; Peng, M.; Liu, J.; de Groot, F. M. F.; Tan, Y. Identifying Electrocatalytic Sites of the Nanoporous Copper-Ruthenium Alloy for Hydrogen Evolution Reaction in Alkaline Electrolyte. *ACS Energy Lett.* **2020**, *5*, 192−199.

(6) Chen, Y.; Ji, S.; Chen, C.; Peng, Q.; Wang, D.; Li, Y. Single-Atom Catalysts: Synthetic Strategies and Electrochemical Applications. *Joule* **2018**, *2*, 1242−1264.

(7) Jiang, K.; Liu, B.; Luo, M.; Ning, S.; Peng, M.; Zhao, Y.; Lu, Y. R.; Chan, T. S.; de Groot, F. M. F.; Tan, Y. Single Platinum Atoms Embedded in Nanoporous Cobalt Selenide as Electrocatalyst for Accelerating Hydrogen Evolution Reaction. *Nat. Commun.* **2019**, *10*, 1743.

(8) Li, Z.; Fu, J. Y.; Feng, Y.; Dong, C. K.; Liu, H.; Du, X. W. A Silver Catalyst Activated by Stacking Faults for the Hydrogen Evolution Reaction. *Nat. Catal.* **2019**, *2*, 1107−1114.

(9) Tavakkoli, M.; Holmberg, N.; Kronberg, R.; Jiang, H.; Sainio, J.; Kauppinen, E. I.; Kallio, T.; Laasonen, K. Electrochemical Activation of Single-Walled Carbon Nanotubes with Pseudo-Atomic-Scale Platinum for the Hydrogen Evolution Reaction. *ACS Catal.* **2017**, *7*, 3121−3130.

(10) Yin, H.; Zhao, S.; Zhao, K.; Muqsit, A.; Tang, H.; Chang, L.; Zhao, H.; Gao, Y.; Tang, Z. Ultrathin Platinum Nanowires Grown on Single-Layered Nickel Hydroxide with High Hydrogen Evolution Activity. *Nat. Commun.* **2015**, *6*, 6430.

(11) Wang, P.; Zhang, X.; Zhang, J.; Wan, S.; Guo, S.; Lu, G.; Yao, J.; Huang, X. Precise Tuning in Platinum-Nickel/Nickel Sulfide Interface Nanowires for Synergistic Hydrogen Evolution Catalysis. *Nat. Commun.* **2017**, *8*, 14580.

(12) Zhang, Z.; Liu, G.; Cui, X.; Chen, B.; Zhu, Y.; Gong, Y.; Saleem, F.; Xi, S.; Du, Y.; Borgna, A.; Lai, Z.; Zhang, Q.; Li, B.; Zong, Y.; Han, Y.; Gu, L.; Zhang, H. Crystal Phase and Architecture Engineering of Lotus-Thalamus-Shaped Pt-Ni Anisotropic Superstructures for Highly Efficient Electrochemical Hydrogen Evolution. *Adv. Mater.* **2018**, *30*, 1801741.

(13) Xu, Y.; Tu, W.; Zhang, B.; Yin, S.; Huang, Y.; Kraft, M.; Xu, R. Nickel Nanoparticles Encapsulated in Few-Layer Nitrogen-Doped Graphene Derived from Metal-Organic Frameworks as Efficient Bifunctional Electrocatalysts for Overall Water Splitting. *Adv. Mater.* **2017**, *29*, 1605957.

(14) Jiang, P.; Chen, J.; Wang, C.; Yang, K.; Gong, S.; Liu, S.; Lin, Z.; Li, M.; Xia, G.; Yang, Y.; Su, J.; Chen, Q. Tuning the Activity of Carbon for Electrocatalytic Hydrogen Evolution *via* an Iridium-Cobalt Alloy Core Encapsulated in Nitrogen-Doped Carbon Cages. *Adv. Mater.* **2018**, *30*, 1705324.

(15) Lei, C.; Wang, Y.; Hou, Y.; Liu, P.; Yang, J.; Zhang, T.; Zhuang, X.; Chen, M.; Yang, B.; Lei, L.; Yuan, C.; Qiu, M.; Feng, X. Efficient Alkaline Hydrogen Evolution on Atomically Dispersed Ni-N_x Species Anchored Porous Carbon with Embedded Ni Nanoparticles by Accelerating Water Dissociation Kinetics. *Energy Environ. Sci.* **2019**, *12*, 149−156.

(16) Zheng, Y. R.; Wu, P.; Gao, M. R.; Zhang, X. L.; Gao, F. Y.; Ju, H. X.; Wu, R.; Gao, Q.; You, R.; Huang, W. X.; Liu, S. J.; Hu, S. W.; Zhu, J.; Li, Z.; Yu, S. H. Doping-Induced Structural Phase Transition in Cobalt Diselenide Enables Enhanced Hydrogen Evolution Catalysis. *Nat. Commun.* **2018**, *9*, 2533.

(17) Subbaraman, R.; Tripkovic, D.; Strmcnik, D.; Chang, K. C.; Uchimura, M.; Paulikas, A. P.; Stamenkovic, V.; Markovic, N. M. Enhancing Hydrogen Evolution Activity in Water Splitting by Tailoring Li^+-Ni $(OH)_2$-Pt Interfaces. *Science* **2011**, *334*, 1256−1260.

(18) Xie, Y.; Cai, J.; Wu, Y.; Zang, Y.; Zheng, X.; Ye, J.; Cui, P.; Niu, S.; Liu, Y.; Zhu, J.; Liu, X.; Wang, G.; Qian, Y. Boosting Water Dissociation Kinetics on Pt-Ni Nanowires by *N*-Induced Orbital Tuning. *Adv. Mater.* **2019**, *31*, 1807780.

(19) Tian, X.; Zhao, X.; Su, Y.; Wang, L.; Wang, H.; Dang, D.; Chi, B.; Liu, H.; Hensen, E. J. M.; Lou, X.; Xia, B. Engineering Bunched Pt-Ni Alloy Nanocages for Efficient Oxygen Reduction in Practical Fuel Cells. *Science* **2019**, *366*, 850−856.

(20) Li, J.; Yin, H. M.; Li, X. B.; Okunishi, E.; Shen, Y. L.; He, J.; Tang, Z. K.; Wang, W. X.; Yücelen, E.; Li, C.; Gong, Y.; Gu, L.; Miao, S.; Liu, L. M.; Luo, J.; Ding, Y. Surface Evolution of a Pt-Pd-Au Electrocatalyst for Stable Oxygen Reduction. *Nat. Energy* **2017**, *2*, 17111.

(21) Snyder, J.; Asanithi, P.; Dalton, A. B.; Erlebacher, J. Stabilized Nanoporous Metals by Dealloying Ternary Alloy Precursors. *Adv. Mater.* **2008**, *20*, 4883−4886.
(22) Strasser, P.; Koh, S.; Anniyev, T.; Greeley, J.; More, K.; Yu, C.; Liu, Z.; Kaya, S.; Nordlund, D.; Ogasawara, H.; Toney, M. F.; Nilsson, A. Lattice-Strain Control of the Activity in Dealloyed Core-Shell Fuel Cell Catalysts. *Nat. Chem.* **2010**, *2*, 454−460.
(23) Li, M.; Duanmu, K.; Wan, C.; Cheng, T.; Zhang, L.; Dai, S.; Chen, W.; Zhao, Z.; Li, P.; Fei, H.; Zhu, Y.; Yu, R.; Luo, J.; Zang, K.; Lin, Z.; Ding, M.; Huang, J.; Sun, H.; Guo, J.; Pan, X.; et al. Single-Atom Tailoring of Platinum Nanocatalysts for High-Performance Multifunctional Electrocatalysis. *Nat. Catal.* **2019**, *2*, 495−503.
(24) Ge, J.; He, D.; Chen, W.; Ju, H.; Zhang, H.; Chao, T.; Wang, X.; You, R.; Lin, Y.; Wang, Y.; Zhu, J.; Li, H.; Xiao, B.; Huang, W.; Wu, Y.; Hong, X.; Li, Y. Atomically Dispersed Ru on Ultrathin Pd Nanoribbons. *J. Am. Chem. Soc.* **2016**, *138*, 13850−13853.
(25) Wang, A.; Li, J.; Zhang, T. Heterogeneous Single-Atom Catalysis. *Nat. Rev. Chem.* **2018**, *2*, 65−81.
(26) van Oversteeg, C. H. M.; Doan, H. Q.; de Groot, F. M. F.; Cuk, T. *In Situ* X-Ray Absorption Spectroscopy of Transition Metal Based Water Oxidation Catalysts. *Chem. Soc. Rev.* **2017**, *46*, 102−125.
(27) Jiang, K.; Luo, M.; Peng, M.; Yu, Y.; Lu, Y. R.; Chan, T. S.; Liu, P.; de Groot, F. M. F.; Tan, Y. Dynamic Active-Site Generation of Atomic Iridium Stabilized on Nanoporous Metal Phosphides for Water Oxidation. *Nat. Commun.* **2020**, *11*, 2701.
(28) Fujita, T.; Guan, P.; McKenna, K.; Lang, X.; Hirata, A.; Zhang, L.; Tokunaga, T.; Arai, S.; Yamamoto, Y.; Tanaka, N.; Ishikawa, Y.; Asao, N.; Yamamoto, Y.; Erlebacher, J.; Chen, M. Atomic Origins of the High Catalytic Activity of Nanoporous Gold. *Nat. Mater.* **2012**, *11*, 775−780.
(29) Zhao, Y.; Luo, M.; Chu, S.; Peng, M.; Liu, B.; Wu, Q.; Liu, P.; de Groot, F. M. F.; Tan, Y. 3D Nanoporous Iridium-Based Alloy Microwires for Efficient Oxygen Evolution in Acidic Media. *Nano Energy* **2019**, *59*, 146−153.
(30) Wang, H.; Luo, Q.; Liu, W.; Lin, Y.; Guan, Q.; Zheng, X.; Pan, H.; Zhu, J.; Sun, Z.; Wei, S.; Yang, J.; Lu, J. Quasi Pd_1Ni Single-Atom Surface Alloy Catalyst Enables Hydrogenation of Nitriles to Secondary Amines. *Nat. Commun.* **2019**, *10*, 4998.
(31) Zhang, X.; Cui, G.; Feng, H.; Chen, L.; Wang, H.; Wang, B.; Zhang, X.; Zheng, L.; Hong, S.; Wei, M. Platinum-Copper Single Atom Alloy Catalysts with High Performance towards Glycerol Hydrogenolysis. *Nat. Commun.* **2019**, *10*, 5812.
(32) Li, J.; Xu, A.; Li, F.; Wang, Z.; Zou, C.; Gabardo, C. M.; Wang, Y.; Ozden, A.; Xu, Y.; Nam, D. H.; Lum, Y.; Wicks, J.; Chen, B.; Wang, Z.; Chen, J.; Wen, Y.; Zhuang, T.; Luo, M.; Du, X.; Sham, T. K.; et al. Enhanced Multi-Carbon Alcohol Electroproduction from CO *via* Modulated Hydrogen Adsorption. *Nat. Commun.* **2020**, *11*, 3685.
(33) Jiang, L.; Liu, K.; Hung, S. F.; Zhou, L.; Qin, R.; Zhang, Q.; Liu, P.; Gu, L.; Chen, H. M.; Fu, G.; Zheng, N. Facet Engineering Accelerates Spillover Hydrogenation on Highly Diluted Metal Nanocatalysts. *Nat. Nanotechnol.* **2020**, *15*, 848−853.
(34) Yang, H. B.; Hung, S. F.; Liu, S.; Yuan, K.; Miao, S.; Zhang, L.; Huang, X.; Wang, H. Y.; Cai, W.; Chen, R.; Gao, J.; Yang, X.; Chen, W.; Huang, Y.; Chen, H. M.; Li, C. M.; Zhang, T.; Liu, B. Atomically Dispersed Ni(I) as the Active Site for Electrochemical CO_2 Reduction. *Nat. Energy* **2018**, *3*, 140−147.
(35) Cao, L.; Luo, Q.; Liu, W.; Lin, Y.; Liu, X.; Cao, Y.; Zhang, W.; Wu, Y.; Yang, J.; Yao, T.; Wei, S. Identification of Single-Atom Active Sites in Carbon-Based Cobalt Catalysts during Electrocatalytic Hydrogen Evolution. *Nat. Catal.* **2019**, *2*, 134−141.

https://dx.doi.org/10.1021/acsnano.0c10885
ACS Nano 2021, 15, 5333−5340